Accuracy improvement of surface measurement through phase correction in spectrally resolved interferometer

Mengsi Zhang [a], Zhiyuan Wang [a], Songjie Luo [a,*], XuanXuan Ji [b], Ziyang Chen [a], Jixiong Pu [a]

[a] *Fujian Provincial Key Laboratory of Light Propagation and Transformation College of Information Science and Engineering, Huaqiao University, Xiamen, Fujian 361021, China*
[b] *Niigata University, Niigata 950-2181, Japan*

ARTICLE INFO

ABSTRACT

The spectrally resolved interferometer (SRI) is used to measure the surface profile by the linear fitting line of its phase distribution of spectral interference signal. However, the noise existed in the phase cannot be ignored if the nano-scale measurement accuracy is required. In this paper, a novel algorithm is proposed to improve the measurement accuracy by using the constant term of linear fitting line of phase distribution in wavenumber domain. The simulations indicate that the algorithm achieves the similar measurement accuracy under the influence of three kinds of noise. Even though the proposed algorithm has the possibility of 4% to bring the additional minor error, it provides a better performance on measurement of entire surface in different SNRs compared with the other two common algorithms. In experiments, the variations of surface less than 10 nm and 30 nm and the repeatability of 2.2 nm and 4.9 nm are obtained in the measurements of a protected aluminium mirror with and without proposed algorithm. A smooth profile with a step shape of nearly 3 μm height is tested, where the maximum repeatability of step height and maximum magnitude of variations of the surfaces reaches to 3.8 nm and 10 nm from the 15.3 nm and 30 nm by using this algorithm. Both the simulations and experimental results demonstrate that the proposed algorithm is feasible for high-precision measurement.

1. Introduction

The rapid progress of manufacturing technology requires an efficient and fast testing process on shape and structure of component to guarantee the production quality. White-light interferometry is applied on the surface measurement because of its high-accuracy and non-contact. As one of the white-light interferometry, the white-light scanning interferometer (WLSI) changes the optical path difference (OPD) by controlling the piezoelectric actuator (PZT) connected to the reference arm. Using a sequence of interferogram captured with the movement of PZT, the surface profile of the object is achieved by the position of the maximum intensity of interference signal or maximum envelope [1–4]. It has been reported that the maximum intensity of interference signal has the better accuracy compared with the maximum envelope. Moreover, the phase-shifting method, which uses the real-valued interference signal, obtains the zero phase nearest to the envelope peak as the reflecting position of measured surface [2]. Performing the Fourier transform on the real-valued interference signal, the complex-valued interference signal in wavenumber domain provides the position of reflecting surface by the slope of linear component of phase distribution [3,5–7]. It re-

duces the requirements for the sampling frequency, and improves the measurement accuracy.

However, the mechanical scanning error of reference mirror limits the measurement accuracy of WLSI [8–11]. The spectrally resolved interferometers (SRI) without the scanning of PZT on the reference arm provides a high data acquisition rate and good sensitive, which make this method widely used for surface or thickness measurements. There are two kinds of SRI depending on the spectral interference signal acquisition style. First kind of SRI is that the wide-band interference signals are separated by grating or prism along the wavelength and detected by the camera [12–14]. Pixels of camera collect signals with different wavelengths. Second kind of SRI adopts a fiber-coupled Fabry-Perot filter or an acousto-optical tunable filter located in front of the wide-band source to generate the tunable spectral element [15–18]. Moreover, the detection system combined with the acousto-optical tunable filter and camera can also collect tunable spectral interference signal [19]. Interferograms with different wavelengths are obtained on different frames. In this manuscript, the first kind of SRI is used to implement measurement.

A series of algorithm had been studied to process the spectral interference signal. Phase-shift algorithm uses the four or more groups of

---

* Corresponding author.
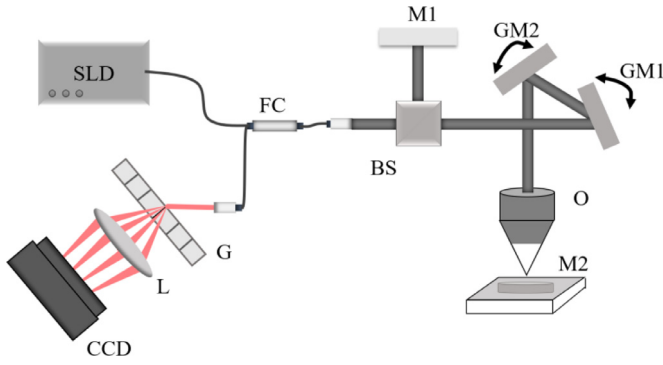 *E-mail address:* songjie@hqu.edu.cn (S. Luo).

Fig. 1. Schematic of a spectrally resolved interferometer. SLD is the superluminescent diode. G is a grating. L is a lens. CCD is a common charge-coupled device. FC is the fiber coupler. BS is the beam-splitter. GM1 and GM2 are the galvanometer to control the direction of the beam. O is an objective lens that focuses the beam on the M2. M1 and M2 are reflecting mirror.

spectral interference signals with constant phase difference to retrieve the shape of specimen [12]. Utilizing polarization camera, the signals with constant phase difference are detected in a single measurement which decrease the mechanical movement error [13]. Phase-shift algorithm requires the exactly phase shift or complicated components to confirm measurement accuracy. Performing the Fourier transform on the spectral interference signal obtained from SRI, the position of reflecting surface of specimen is given by the location of maximum value of amplitude distribution [14,17,19]. However, the insufficient precision of this algorithm limits its application for high accuracy measurement. By selecting the region of Fourier transformed spectral interference signal with dominant amplitude, inverse Fourier transform is carried out to obtain the phase distribution in wavenumber domain [15,16,18]. The slope of phase distribution provides a more exact position of reflecting surface.

According to our investigation, the constant term of linear fitted phase in wavenumber domain (CLPW) has the ability to further improve the measurement accuracy [20–22].Thus, an algorithm is proposed to the surface measurement on SRI in this paper. Three kinds of additive noise are added in simulation to prove that the CLPW can reduce the measurement error in SRI. Even though the CLPW has the 4% proba-

bility to bring additional minor error, the entire performance of CLPW improves the measurement accuracy. Moreover, a flat reflecting mirror and a flat surface with a step shape of nearly 3 μm height are used as the specimens in SRI. The measurement results corrected by CLPW provide a better flatness and repeatability, which agrees with the simulation result.

2. Principles

The experimental setup is illustrated in Fig. 1, in which a superluminescent diode (SLD) is the light source. The positions of measured mirror and reference mirror are denoted as z_0 and z_1, and the OPD is $\Delta z=z_0$-z_1. The spectral resolved interference signal detected by this system is simply given by

$$S(\sigma) = I_0(\sigma) + I_1(\sigma)\cos[4\pi\Delta z\sigma] + N_b(\sigma), \tag{1}$$

where $I_0(\sigma)$ is spectral intensity of the two beams directly reflected from the reference and specimen, and $I_1(\sigma)$ is the visibility function. $\sigma=1/\lambda$ is the wavenumber. $N_b(\sigma)$ is the additive noise from electric devices, SLD light source and the beams reflected by the optical surface in the fiber or lenses. The Fourier transform (FT) of interference term of Eq. (1) in the region of positive spatial domain is derived as

$$F(z) = \int_{-\infty}^{\infty} I_1(\sigma)\exp[-j\cdot 4\pi(z-\Delta z)\sigma]d\sigma + n(z), (z > 0), \tag{2}$$

where the $n(z)$ is expressed as the Fourier transform of $N_b(\sigma)$. Regarding the Δz as the modulation frequency of spectral resolved interference signal in Eq. (1), z is its frequency. Inverse Fourier transform (IFT) of Eq. (2) is given by

$$S_c(\sigma) = I_F(\sigma)\exp[j\cdot 4\pi\Delta z\sigma]\exp[j\beta(\sigma)], \tag{3}$$

The part of frequency component of $n(z)$, that overlap the frequency of interference signal component in Eq. (2), has an influence on the phase distribution in Eq. (3), expressed as $\beta(\sigma)$. Denoting the linear component of phase in Eq. (3) as $a_0+a_1\sigma$, the OPD is provided through the $a_1=4\pi\Delta z$, ignoring the noise of $\beta(\sigma)$. The position of reflecting surface is regarded as

$$z_s = a_1/(4\pi), \tag{4}$$

The $\beta(\sigma)$ contains the complicated components can be expressed as a polynomial $b_0+b_1\sigma+b_2\sigma^2 + b_3\sigma^3+...$, where the b_0, b_1, b_2, b_3...are coefficients. Thus, the slope of linear component $a_0+a_1\sigma$ of $4\pi\Delta z\sigma+\beta(\sigma)$
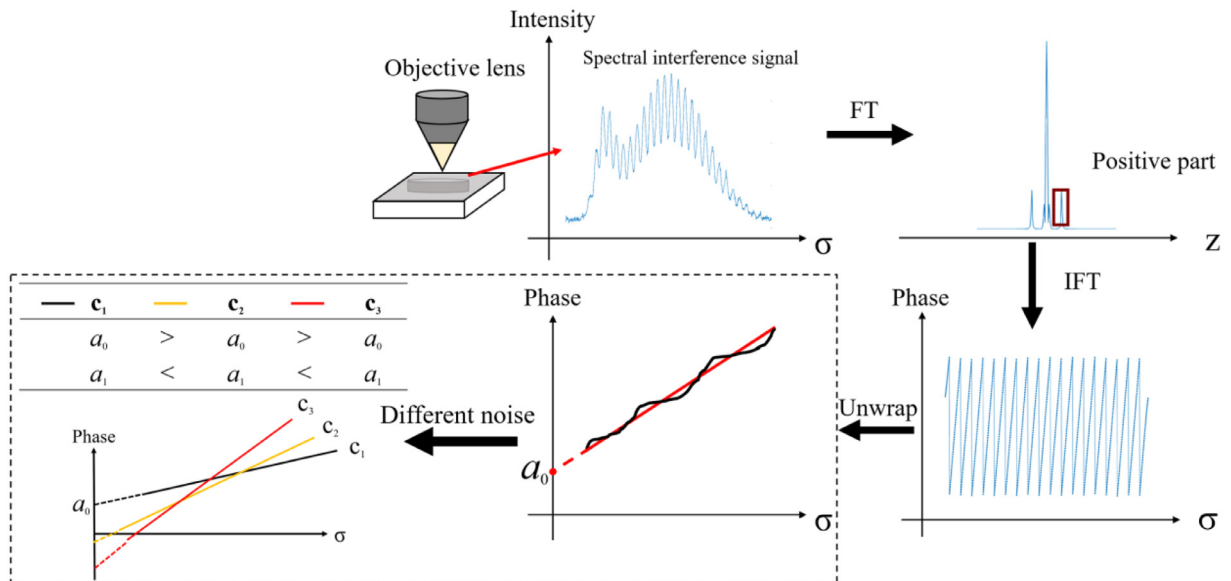

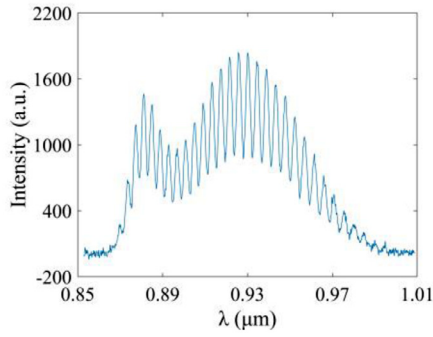**Fig. 2.** The main procedures of the proposed algorithm.

Fig. 3. Spectral interference signal in simulation.

cannot provide the exact value of $4\pi\Delta z$ anymore, which move the value of z_s away from Δz unavoidably. Here, the position of reflecting surface obtained by adding CLPW of a_0 is proposed as

$$z_p = a_1/(4\pi) + a_0\lambda_A/(4\pi). \tag{5}$$

where λ_A is the average wavelength of $I_F(\sigma)$.

Fig. 2 shows the main procedures of proposed algorithm. After the FT and IFT of spectral interference signal, the unwrapped phase and its linear fitting line are shown by black and red solid lines. Performing the different noise $N_b(\sigma)$ on the spectral interference signal, the expected linear fitted phase distributions are shown as C_1, C_2 and C_3, whose a_0 and a_1 have the opposite change trend. In this way, the a_0 has the possibility to reduce the measurement error in z_p. The a_0 may bring the additional error for z_p if the a_0 and a_1 have same change trend. Thus, a simulation is carried out to investigate the following questions.

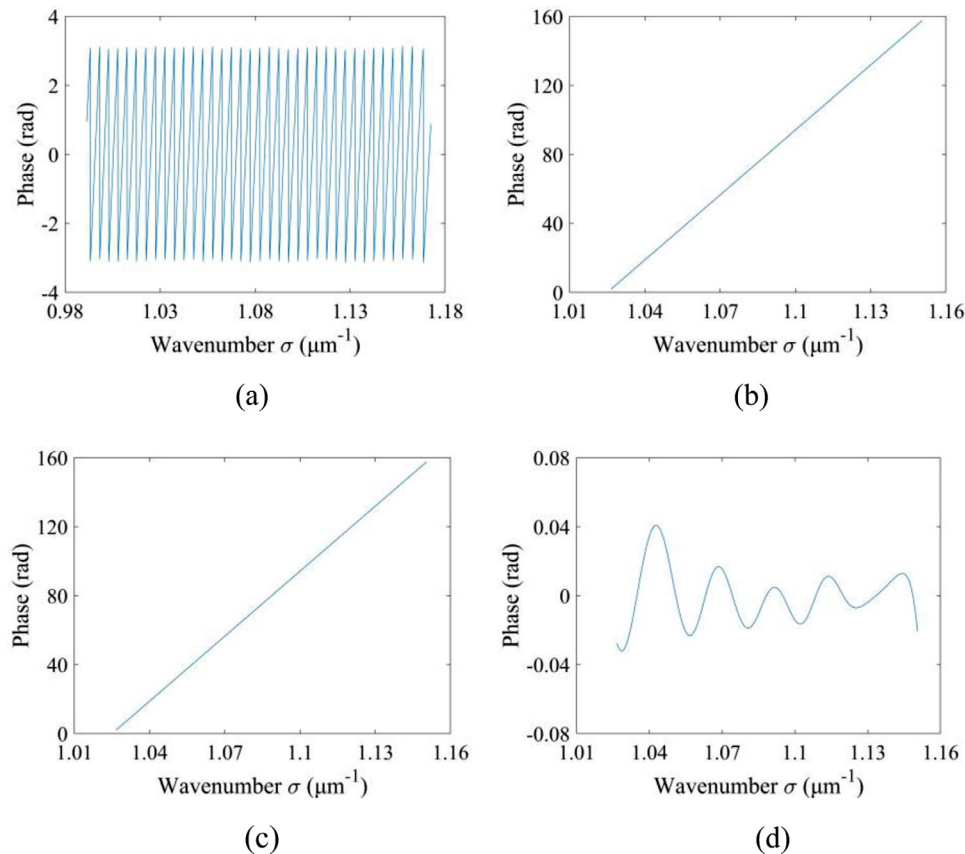*Q1*: Does the z_p have better performance than z_s?

Q2: If z_p has the worse performance than z_s, how a_0 affects the final measurement result obtained from z_p?

3. Simulation

The spectral intensity of SLD in experiment was used to generate the spectral interference signal. Considering the complicated components of additive noise, the Gaussian noise, Poisson noise and random noise were regarded as $N_b(\sigma)$ in the simulation, respectively. First, the Gaussian noise with averaged value of 0 nm was used to explain the simulation process. Fig. 3 shows the spectral interference signal generated with $\Delta z = 100$ μm, sampling point $N = 2048$, sampling interval $\Delta\lambda = 0.0761$ μm and the Gaussian noise with SNR=20 dB. Fourier transform was performed on the spectral interference signal to obtain the complex-valued signal in spatial domain after converting its wavelength to wavenumber and interpolation with constant sampling interval. The complex-valued white-light interference signal in wavenumber domain was obtained by inverse Fourier transform of positive interference part in spatial domain selected by rectangular filter. Fig. 4(a), (b) show the phase and unwrapped phase distribution of the signal in Fig. 3. The linear and nonlinear part of unwrapped phase obtained by linear fitting method are shown in Fig. 4(c), (d). And the values of a_0 and a_1 are given by phase in Fig. 4(c).

In order to solve Q1, 100,000 groups of Gaussian noise $N_b(\sigma)$ were added to obtain the z_s and z_p. The error generated by noise are denoted as $\Delta z_s = z_s - \Delta z$ and $\Delta z_p = z_p - \Delta z$. Fig. 5 shows the statistical diagram whose abscissa are the values of Δz_s and Δz_p and ordinate is the number of Δz_s and Δz_p distributed in each interval. The Δz_s and Δz_p are mainly distributed in the region of $[-0.06$ μm0.06 μm$]$ and $[-0.003\mu$m 0.003μm$]$, respectively. It indicates that z_p has the higher possibility to own less measurement error than the value of z_s in SRI.

As the Eq. (5) shows, the z_p has the worse performance than z_s if the a_0 and a_1 have same change trend. In order to solve Q2, the varia-
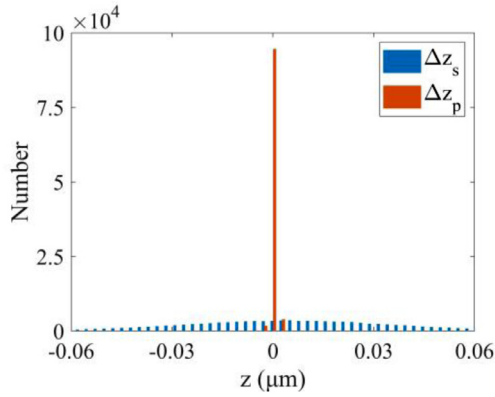

(a)

(b)

(c)

(d)

Fig. 4. Procedures to achieve the value of a_0 and a_1. (a) Phase of spectral interference signal in wavenumber domain. (b) Unwrapped phase distribution of (a). (c) Linear component of (b). (d) Non-linear component of (b).

Fig. 5. Histogram of Δz_s and Δz_p value distributions using Gaussian noise.

tion on a_0 and a_1 generated by noise are denoted as the Δa_0 and Δa_1 to investigate the characteristic of z_p. The change trend of a_0 and a_1 is determined by the symbol of $\Delta a_0 \times \Delta a_1$. Fig. 6(a) shows the statistical chart of the symbol of $\Delta a_0 \times \Delta a_1$, in which the $\Delta a_0 \times \Delta a_1 < 0$ and $\Delta a_0 \times \Delta a_1 > 0$ representing the opposite and same change trend of a_0 and a_1, respectively. It is made clear that z_p has the possibility of 96% to reduce the error in z_s. Unexpectedly, the z_p has the possibility of 4% to enlarge the measurement error in z_s.

Since the z_p has 4% possibility to bring additional error for the surface measurement, it is important to analyze the detailed error caused by the a_0. In Eq. (5), the term of $a_0 \frac{\lambda_A}{4\pi}$ generates the difference between z_s and z_p. Thus, the distribution of $|a_0 \frac{\lambda_A}{4\pi}|$ is given in Fig. 6(b), whose abscissa is the value of $|a_0 \frac{\lambda_A}{4\pi}|$ and ordinate is the number of $|a_0 \frac{\lambda_A}{4\pi}|$ distributed in each interval. In the conditions of $\Delta a_0 \times \Delta a_1 < 0$ and $\Delta a_0 \times \Delta a_1 > 0$, the maximum values of $|a_0 \frac{\lambda_A}{4\pi}|$ are less than 100 nm and 6 nm, and the average values of $|a_0 \frac{\lambda_A}{4\pi}|$ are 25.4 nm and 3.7 nm, respectively.

In order to analysis the noise resistance of the algorithm for other kinds of noise, the Poisson noise and random noise with SNR=20dB were used as additive noise $N_b(\sigma)$. Fig. 7 shows the histogram of Δz_s and Δz_p retrieved from 100,000 groups of $N_b(\sigma)$. Δz_s and Δz_p are mainly distributed in the region of $[-0.06 \ \mu m \ 0.06 \ \mu m]$ and $[-0.003 \mu m \ 0.003 \mu m]$ in Fig. 7, respectively. Fig. 8 shows the statistical charts of the symbol of $\Delta a_0 \times \Delta a_1$ obtained from the Poisson noise and random noise. From Fig. 8(a) and (c), the z_p has the possibility of 96% to reduce the error and the possibility of 4% to enlarge the measurement error in z_s under the influence of Poisson noise and random noise. Fig. 8(b) and (d) show that the maximum values of $|a_0 \frac{\lambda_A}{4\pi}|$ in conditions of $\Delta a_0 \times \Delta a_1 < 0$
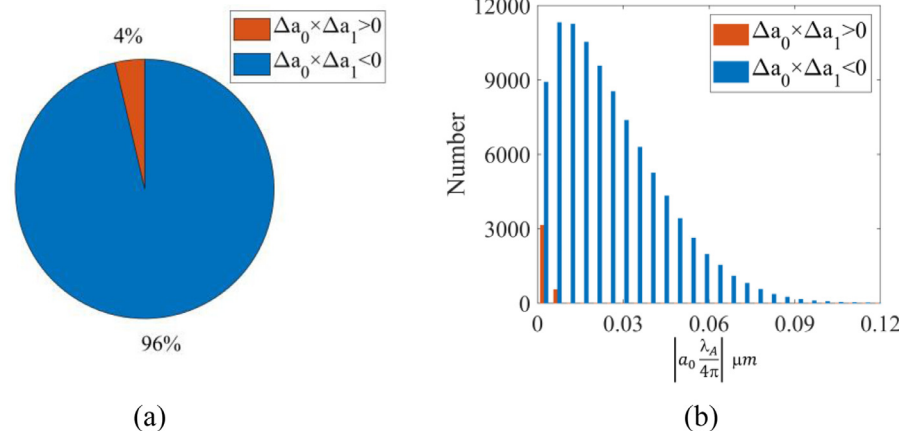
and $\Delta a_0 \times \Delta a_1 > 0$ are less than 100 nm and 6 nm. The average value of $|a_0 \frac{\lambda_A}{4\pi}|$ affected by Poisson noise in the conditions of $\Delta a_0 \times \Delta a_1 < 0$ and $\Delta a_0 \times \Delta a_1 > 0$ are 25.4 nm and 3.6 nm, respectively. And the average value of $|a_0 \frac{\lambda_A}{4\pi}|$ affected by random noise in the conditions of $\Delta a_0 \times \Delta a_1 < 0$ and $\Delta a_0 \times \Delta a_1 > 0$ are 25.5 nm and 3.7 nm.

An irregular surface in Fig. 9(a) with 40×40 values was generated to test the surface reconstruction ability of the algorithm. Gaussian noise, Poisson noise and random noise with SNR=20 dB were used in simulation. The z_a is position of the maximum amplitude of Fourier transformed spectral interference signal. The reconstructed surfaces achieved by three algorithms are given in Fig. 9. Fig. 9(b–d) are surfaces obtained by z_a, z_s and z_p in the case of Gaussian noise. Since the vertical resolution of z_a is about 2.7 μm, it is impossible to measure the surface with the variation less than 0.4 μm in Fig. 9(a). Thus, the surface obtained by the z_a in Fig. 9(b) is a flat surface, and the Fig. 9(e) and (h) have the same condition with Fig. 9(b). Fig. 9(e–g) and (h–j) are reconstructed surfaces in the conditions of Poisson noise and random noise, respectively. It is made clear that the surface retrieved by z_p is closer to original surface than z_s.

The difference between the reconstructed surfaces and original surface indicates the reconstruction error of the algorithms. By subtracting original surface profile of Fig. 9(a) from reconstructed surfaces with different SNRs, its line distributions along $Y = 20$ are shown in Fig. 10. Fig. 10(a), (c) and (e) show the difference obtained by z_s in the conditions of the Gaussian noise, Poisson noise and random noise with SNR=10 dB, 20 dB and 30 dB. Fig. 10(b), (d) and (f) show the difference obtained by z_p, whose reconstructed error is less than 6 nm. The reconstructed error of z_p is significantly lower than result retrieved by z_s. Table 1 gives the standard deviation of reconstructed error of entire surface caused by three kinds of noise with different SNRs. Reconstruction error obtained by z_s and z_p both decrease with the increase of SNR. The similar standard deviations of reconstruction error obtained by three kinds of noise in same SNR demonstrate that different noise has the similar effect on the algorithm. And the standard deviations obtained by z_p are always less than that of z_s, which prove that the z_p has a better noise resistance.

In conclusion, when the Gaussian noise, Poisson noise and random noise with SNR=20 dB are used in simulation, the z_p has the possibility of 96% to reduce the average error of 25.4–25.5 nm, however, it also has the possibility of 4% to enlarge the average error of 3.6–3.7 nm in z_s. An irregular surface is used to compare the reconstruction error of three algorithms. As shown in Figs. 9 and 10, the reconstructed surface obtained by z_p has a better performance than z_s. The standard deviation of reconstructed error in Table 1 also indicates that profiles achieved by z_p have strong ability of noise immunity. It is made clear that proposed algorithm using CLPW can improve the surface measurement accuracy in SRI.
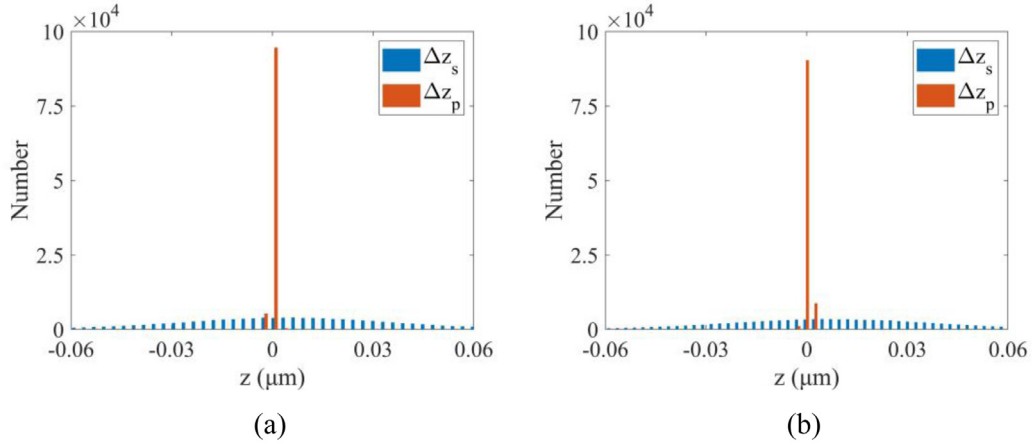

(a)

(b)

Fig. 6. Statistical diagram of the effect of Gaussian noise on a_0 and a_1. (a) The diagram of proportion of $\Delta a_0 \times \Delta a_1 < 0$ and $\Delta a_0 \times \Delta a_1 > 0$. (b) The histogram of $|a_0 \frac{\lambda_A}{4\pi}|$ in the conditions of $\Delta a_0 \times \Delta a_1 < 0$ and $\Delta a_0 \times \Delta a_1 > 0$.

Fig. 7. Histograms of Δz_s and Δz_p distributions by using (a) Poisson noise and (b) random noise.
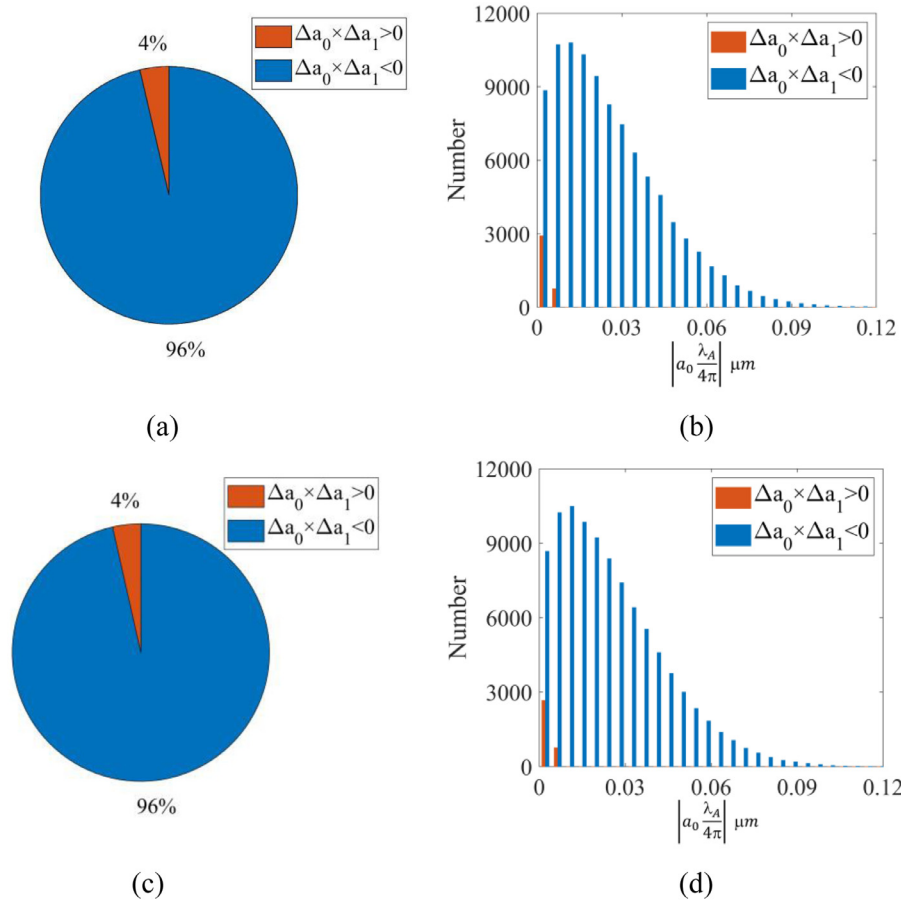

Fig. 8. Statistical diagrams of the effect of noise on a_0 and a_1. (a) The diagram of proportion of $\Delta a_0 \times \Delta a_1 < 0$ and $\Delta a_0 \times \Delta a_1 > 0$ using Poisson noise. (b) The histogram of $|a_0 \frac{\lambda_A}{4\pi}|$ in the conditions of $\Delta a_0 \times \Delta a_1 < 0$ and $\Delta a_0 \times \Delta a_1 > 0$ using Poisson noise.(c) The diagram of proportion of $\Delta a_0 \times \Delta a_1 < 0$ and $\Delta a_0 \times \Delta a_1 > 0$ using random noise. (d) The histogram of $|a_0 \frac{\lambda_A}{4\pi}|$ in the conditions of $\Delta a_0 \times \Delta a_1 < 0$ and $\Delta a_0 \times \Delta a_1 > 0$ using random noise.

Table 1
Standard deviation of reconstructed error of surface caused by three kinds of noise with different SNRs.

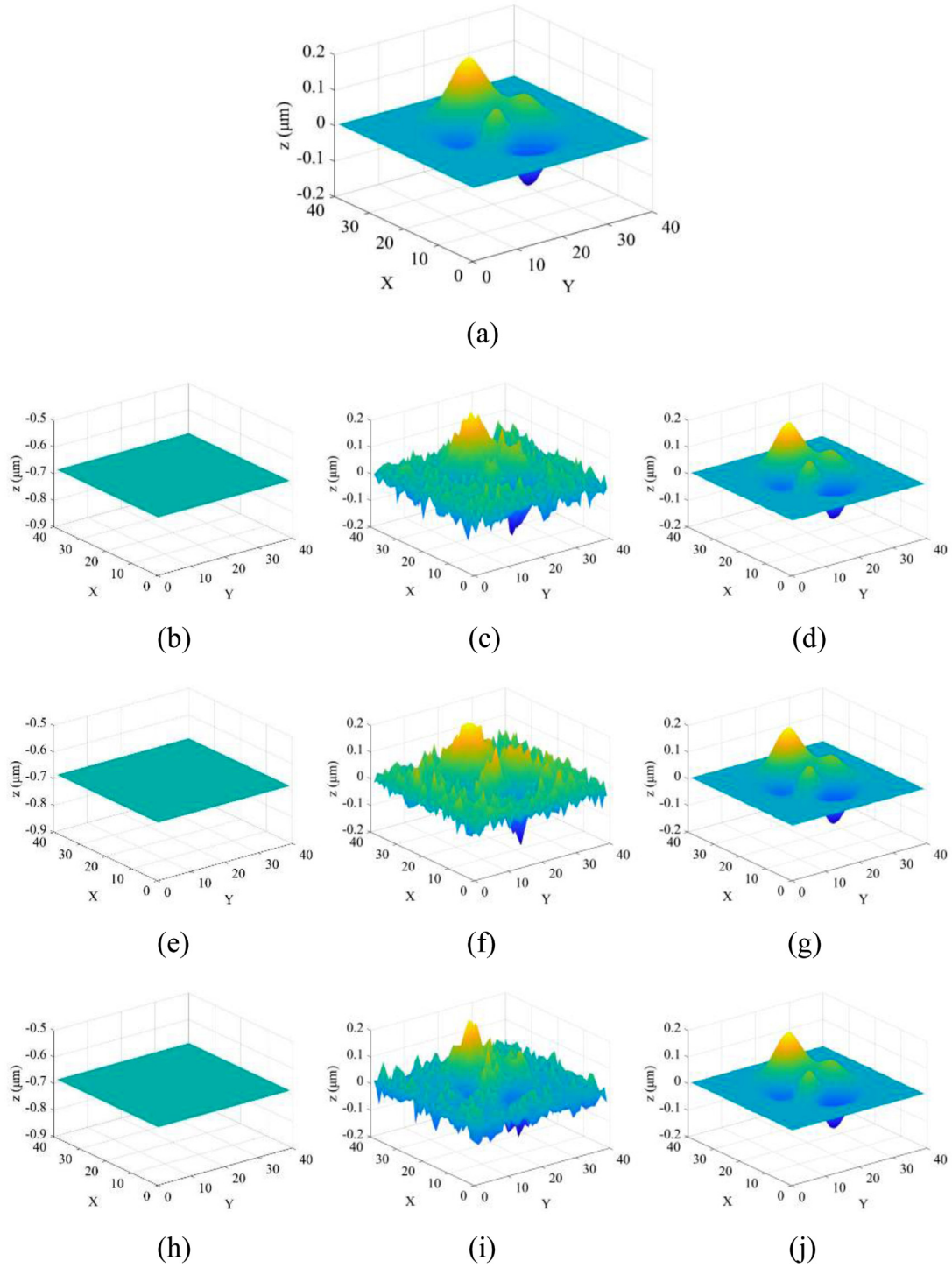| Standard deviation of reconstruction error	SNR(dB)	Gaussian noise	Poisson noise	Random noise
z_s(nm)	10	90.02	84.66	86.17
	20	25.30	28.09	29.65
	30	10.42	11.24	9.80
z_p(nm)	10	2.53	2.31	2.35
	20	0.76	0.75	0.68
	30	0.30	0.28	0.30

Fig. 9. The surface reconstruction by three kinds of algorithms. (a) An original irregular surface (b–d) Reconstructed surface from z_a, z_s and z_p affected by Gaussian noise. (e–g) Reconstructed surface from z_a, z_s and z_p affected by Poisson noise. (h–j) Reconstructed surface from z_a, z_s and z_p affected by random noise.

4. Experiment

Fig. 1 shows the SRI setup. The integrated system (OCTP-900/M, Thorlabs Inc.) contained the spectral analyzer and the light source of SLD. Fig. 11 shows the spectrum distribution of SLD with the region of 853-1008 nm. The light beam was collimated and coupled to the Michelson interferometer after coming out from the fiber. The reference beam was reflected by the stable mirror M_1. The sample light was reflected by

the measured flat mirror M_2, after passing through a pair of galvanometer scanners and an objective lens. An interference signal in Fig. 12 was collected by the detection system, built by the grating, lens and CCD. Measurement region of 50×50 μm was scanned with the lateral measurement resolution of 0.1 μm by the frequency of 100 KHz. Since the measurement area was not large, the dispersion phase generated by the experimental setup was regarded same in all the interference signals, which made the effect of dispersion phase negligible. The spectral data
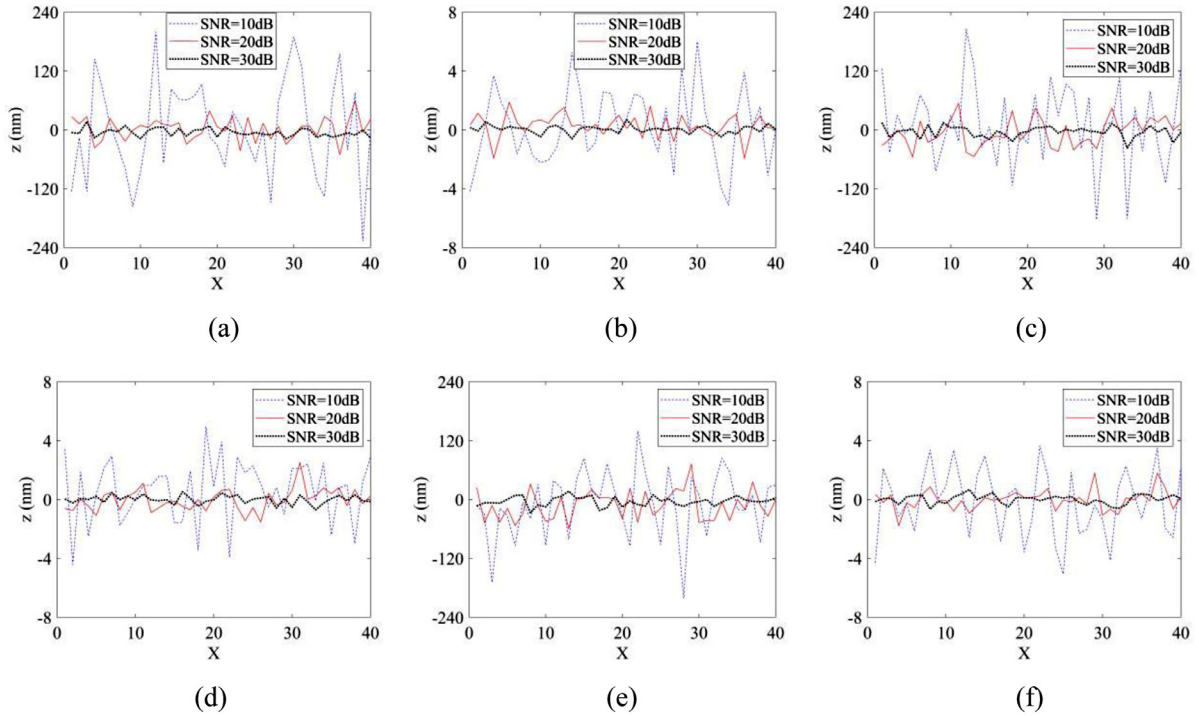
Fig. 10. Line distributions at Y=20 of the difference between the reconstructed surfaces and the original surface in different SNRs.(a, b) Line distributions obtained by z_s and z_p in the case of Gaussian noise. (c, d) Line distributions obtained by z_s and z_p in the case of Poisson noise. (e, f) Line distributions obtained by z_s and z_p in the case of random noise.
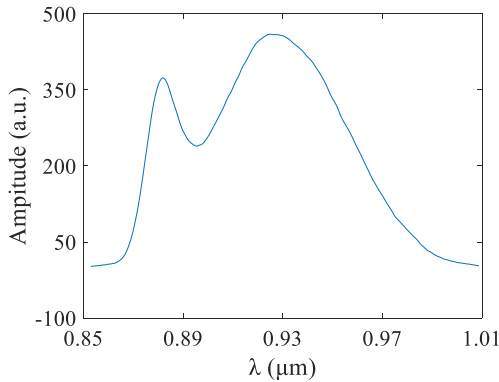

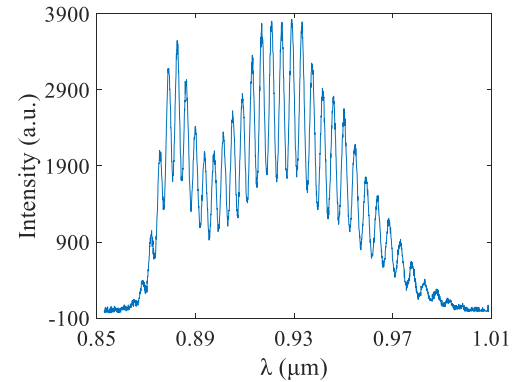**Fig. 11.** The spectrum of light source.

Fig. 12. Spectral interference signal captured by the experimental setup.

of an interference signal from CCD had 2048 elements, which generated the three-dimensional structural data of $500 \times 500 \times 2048$ voxels in one measurement.

Performing the process described in Section 2 on the detected interference signal, the values of z_s and z_p of each measurement point were obtained by the Eqs. (4),(5). Fig. 13 shows the surface profiles obtained by the values of z_s and z_p, where the tilt and piston component are eliminated. The measurement points are denoted by X and Y, where the X and Y were from 1 to 500. It is shown that the measured surface of z_p is smoother than that of z_s. In order to show clearly the variation of surface profile, the cross sections of $X = 250$ and $Y = 250$ of the surface distributions in Fig. 13 are given by Fig. 14. The magnitude of variations of z_p are less than that of z_s, and the maximum magnitude of them are about 30 nm and 10 nm, respectively. Fig. 15 shows the difference between two groups of measured surfaces. Variations of most measurement points in Fig. 15(a) are larger than that of Fig. 15(b), which indicates that two surfaces obtained from z_p at different measurement time have the less error. The repeatability was denoted by calculating a root-

mean-square value of difference between ten surface profiles in different measurements. The repeatability is 2.2 nm in measurement obtained from z_p, while it is 4.9 nm in the measurement obtained from z_s.

A smooth profile with a step shape of nearly 3 μm height was measured as shown in Fig. 16. Most positions of upper and lower surfaces in Fig. 16 are flat, excepted the jumps close to the edge of the step discontinuity. Those jumps are called the batwing effect, which usually appear at the edge of the step if the step height is smaller than the coherence length of light source. It also increases with rise of the numerical aperture of the objective. The diffraction models were proposed to explain the batwing effect [23,24]. Here, we removed the batwings effect by replacing the unreasonably high and low points close to the step with adjacent reasonable points to achieve the measurement at the edge. Fig. 17 shows the cross sections of X=100, 200 and 300 of the surface distributions. The points of Y=156 and Y=186 of cross sections of X=100, 200 and 300 are chosen to retrieve the step height. Since the measurement results are similar in ten measurements, Table 2 gives the step height measurement results of three measurements denoted as M$_1$,
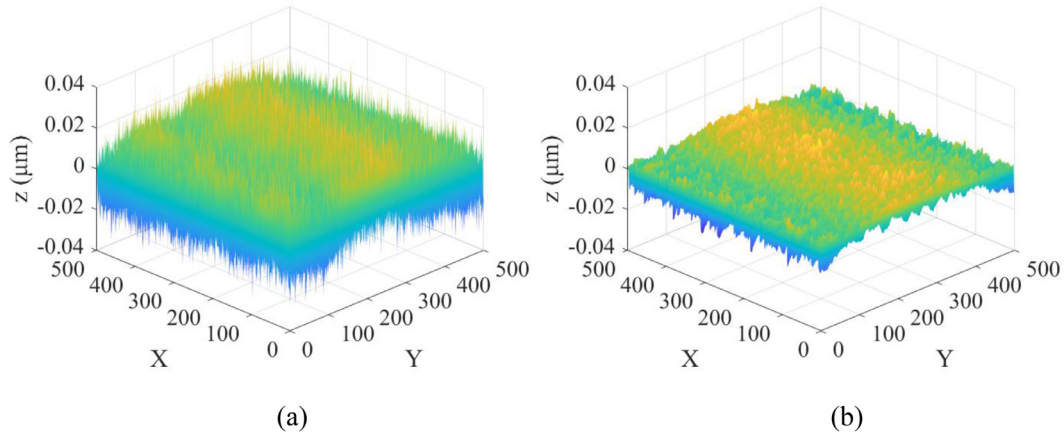
Fig. 13. Surface profiles obtained from the measured values of (a) z_s and (b) z_p.
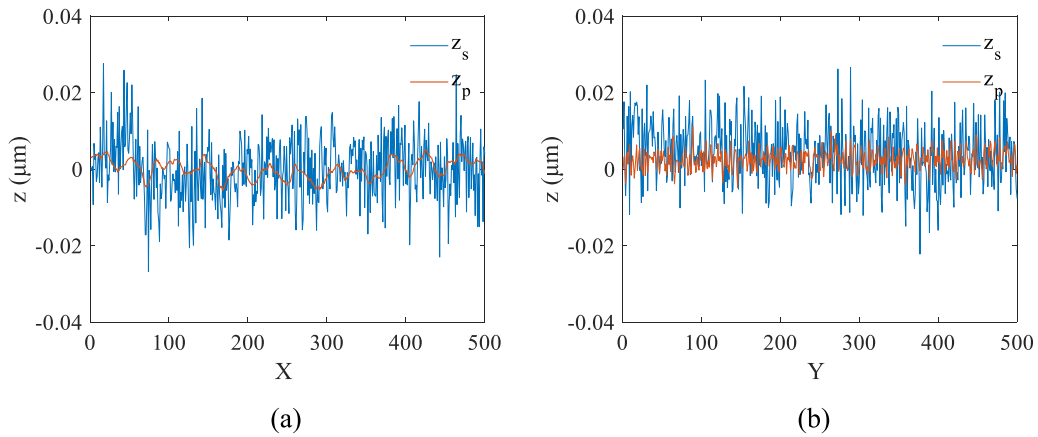

Fig. 14. The cross sections of the measured surfaces in Fig. 13 at (a) Y=250 along X direction and (b) X=250 along the Y direction.
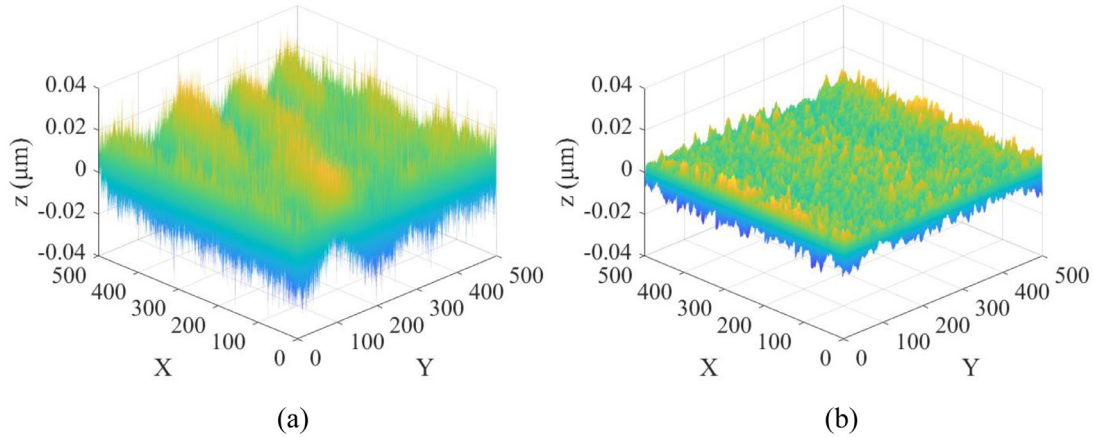

Fig. 15. Difference between the surface profiles in two measurements obtained from (a) z_s and (b) z_p.

Table 2
Step height obtained from three measurements.

Measurement sequences	X=100		X=200		X=300	
	$z_s(\mu m)$	$z_p(\mu m)$	$z_s(\mu m)$	$z_p(\mu m)$	$z_s(\mu m)$	$z_p(\mu m)$
M_1	2.8764	2.9232	2.8876	2.9236	2.9246	2.9288
M_2	2.9004	2.9282	2.9149	2.9255	2.9294	2.9312
M_3	2.8939	2.9207	2.8892	2.9224	2.9239	2.9310
Average value	2.8902	2.9240	2.8972	2.9238	2.9260	2.9303
Standard deviation	0.0124	0.0038	0.0153	0.0016	0.0030	0.0013

M_2 and M_3. From Table 2, the average values of height retrieved from the z_s are farther from 3 μm compared with z_p. The smaller values of standard deviation of height obtained from z_p indicate that z_p provides a better repeatability on the step height measurements. Line distributions of X=1–150 and X=200–400 of Fig. 17(b) are selected to show the variations of surface clearly after elimination of its tilt and piston component in Fig. 18. The maximum magnitude of variations of z_p and z_s are less than 10 nm and 30 nm, which are similar with the result obtained from the reflecting mirror. The experimental results of surface and step
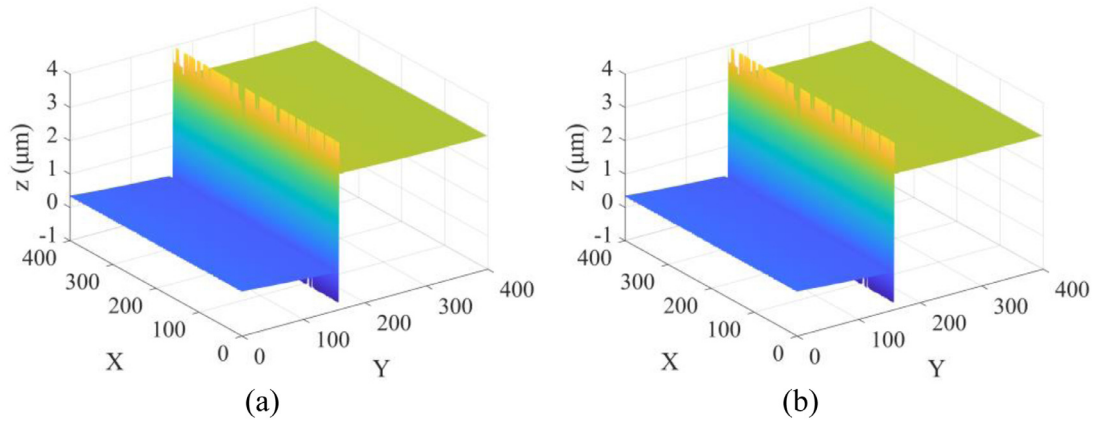
Fig. 16. The surface profiles with a step shape obtained from the measured values of (a) z_s and (b) z_p.
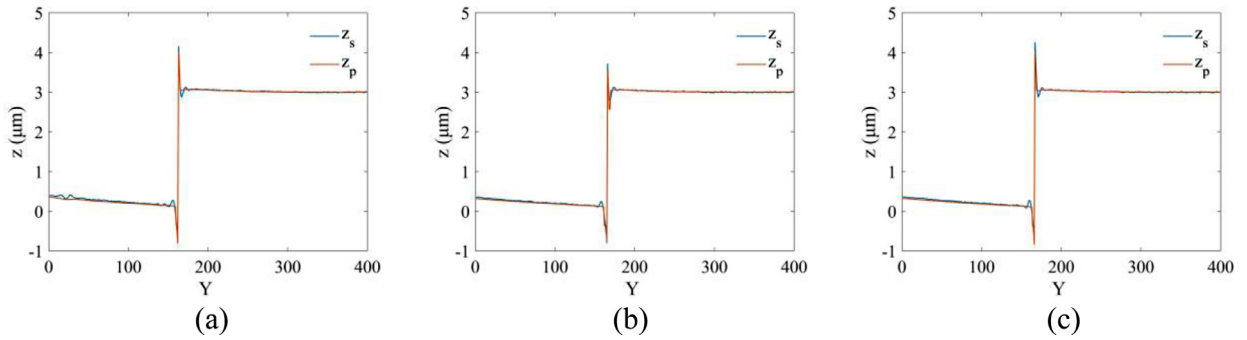

Fig. 17. The cross sections of the measured surfaces in Fig. 16 at (a) X=100, (b) X=200 and (C) X=300 along Y direction.
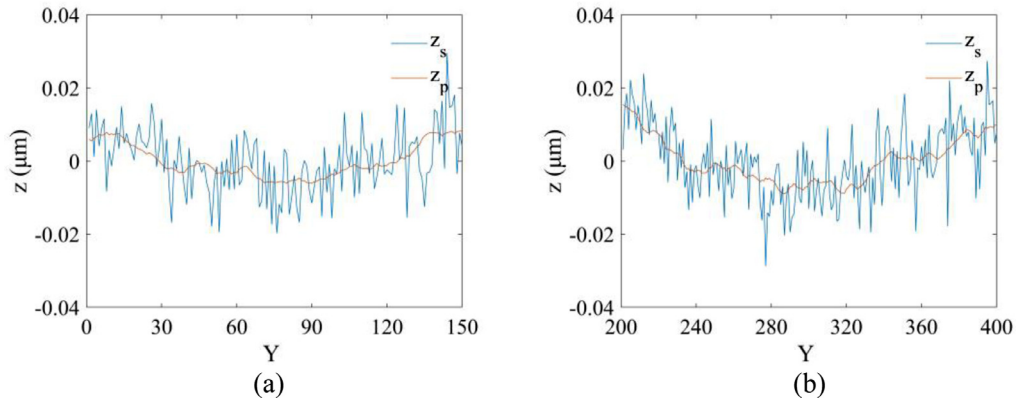

Fig. 18. The cross sections of Fig. 17(b) at X=200 in the region of (a) Y=1–150 and (b) Y=200–400 after removing its tilt and piston component.

height measurements demonstrate that the reconstructed profile from z_p provides a higher measurement accuracy than that from z_s in SRI.

5. Conclusion

In this paper, a novel spectral interference signal processing algorithm is proposed to improve the surface measurement accuracy in SRI. Three kinds of noise are added in the simulation to verify that the CLPW has prominent noise resistance ability. Even though there is possibility of 4% for CLPW to bring additional minor error, the CLPW brings the good measurement accuracy and repeatability for the entire surface measurement. After the algorithm is deployed on measurement of a flat mirror in experiment, the maximum variation of the surface and the repeatability are optimized to 10 nm and 2.2 nm from 30 nm and 4.9 nm, respectively. The measurement results of a smooth profile with a step shape

of nearly 3 μm height show that the algorithm using CLPW gives the good surface variation of 10 nm and step height repeatability of 3.8 nm. Our work reveals the characteristic of CLPW, and provides the surface measurement method with high accuracy and speed.

Declaration of Competing Interest

The authors declare that they have no known competing financial interests or personal relationships that could have appeared to influence the work reported in this paper.

CRediT authorship contribution statement

Mengsi Zhang: Methodology, Software, Investigation, Writing – original draft. **Zhiyuan Wang:** Methodology, Software, Writing – re-

view & editing. **Songjie Luo:** Conceptualization, Formal analysis, Writing – original draft, Writing – review & editing. **XuanXuan Ji:** Software. **Ziyang Chen:** Formal analysis, Validation. **Jixiong Pu:** Supervision, Writing – review & editing.

Data availability

Data will be made available on request.

Funding

References

[1] Park MC, Kim SW. Direct quadratic polynomial fitting for fringe peak detection of white light scanning interferograms. Opt Eng 2000;39(4):952–9.

[2] Harasaki A, Schmit J, wyant JC. Improved vertical-scanning interfermetry. Appl Opt 2000;39(13):2107–15.

[3] de Groot P, de Lega XC, Kramer J, Turzhitsky M. Determination of fringe order in white-light interference microscopy. Appl Opt 2002;41(22):4571–8.

[4] Pikálek T, Fořt T, Buchta Z. Detection techniques in low-coherence interferometry and their impact on overall measurement accuracy. Appl Opt 2014;53(36):8463–70.

[5] de Groot P, Deck L. Surface profiling by analysis of white-light interferograms in the spatial frequency domain. J Mod Opt 1995;42(2):389–401.

[6] Sinclair MB, de Boer MP, Corwin AD. Long-working-distance incoherent-light interference microscope. Appl Opt 2005;44(36):7714–21.

[7] Luo S, Sasaki O, Chen Z, Pu J. Utilization of complex-valued signals in a white-light scanning interferometer for accurate measurement of a surface profile. Appl Opt 2017;56(15):4419–25.

[8] Ai C, Wyant JC. Effect of piezoelectric transducer nonlinearity on phase shift interferometry. Appl Opt 1987;26:1112–16.

[9] Ma L, Zhao Y, Du M, et al. Phase error compensation based surface recovery algorithm using spectrum selection for white light interferometry. Appl Opt 2021;60(21):6063 -6043.

[10] Kim N, Kwon S. Correction of PZT scanner errors using a phase compensation method in white-light phase-shifting interferometry. Appl Opt 2021;60:9311–18.

[11] Ma L, Zhao Y, Pei X, Liu YZ, Sun FM, Wu S. Phase noise estimation based white light scanning interferometry for high-accuracy surface profiling. Opt Express 2022;30:11912–22.

[12] Ghim YS, Rhee HG, Davies A. Simultaneous measurements of top surface and its underlying film surfacesin multilayer film structure. Sci Rep 2017;7(1):11843.

[13] Ghim YS, Seo YB, Joo KN, Rhee HG. Single-shot spectrally-resolved interferometry for the simultaneous measurement of the thickness and surface profile of multilayer films. Opt Express 2021;29(16):25524–34.

[14] Costantino S, Martinez OE. Wide band interferometry for thickness measurement. Opt Express 2003;11(8):952–7.

[15] Ghim YS, Rhee HG, Yang HS, Lee YW. Thin-film thickness profile measurement using a Mirau-type low-coherence interferometer. Meas Sci Technol 2013;24(7):075002.

[16] Sarunic MV, Weinberg SH, Izatt JA. Full field swept sourcephase microscopy. Opt Lett 2006;31:1462–4.

[17] Považay B, Unterhuber A, Hermann B, Sattmann H, Arthaber H, Drexler W. Full-field time-encoded frequency-domain opticalcoherence tomography. Opt Express 2006;14:7661–9.

[18] Gao F, Muhamedsalih H, Qian X. Surface and thickness measurement of a transparent film using wavelength scanning interferometry. Opt Express 2012;20(19):21450–6.

[19] Machikhin AS, Pozhar VE, Viskovatykh AV, Burmak LI. Acousto-optical tunable filter for combined wideband, spectral, and optical coherence microscopy. Appl Opt 2015;54:7508–13.

[20] Luo S, Sasaki O, Chen Z, Choi S, Pu J. Exact surface profile measurement without subtracting dispersion phase through Fourier transform in a white-light scanning interferometer. Appl Opt 2018;57(4):894–9.

[21] Luo S, Suzuki T, Sasaki O, Choi S, Chen Z, Pu J. Signal correction by detection of scanning position in a white-light interferometer for exact surface profile measurement. Appl Opt 2019;58(13):3548–54.

[22] Luo S, Sasaki O, Choi S, Suzuki T, Chen Z, Pu J. Shape measurement of a thin glass plate through analyzing dispersion effects in a white-light scanning interferometer. Opt Lasersin Eng 2021;139(7):106505.

[23] Harasaki A, Wyant JC. Fringe modulation skewing effect in white-light vertical scanning interferometry. Appl Opt 2000;39:2101–6.

[24] Xie W, Lehmann P, Niehues J. Lateral resolution and transfer characteristics of vertical scanning white-light interferometers. Appl Opt 2012;51:1795–803.